Supplement of Atmos. Chem. Phys., 25, 12811–12830, 2025
https://doi.org/10.5194/acp-25-12811-2025-supplement

Atmospheric Chemistry and Physics
Open Access

Supplement of

Divergent changes in aerosol optical hygroscopicity and new particle formation during a heatwave of summer 2022

Yuhang Hao et al.

Correspondence to: Jing Chen (chen.jing@cqu.edu.cn)

S1. Site description

The observation site was located on the rooftop of a building (~15 m above the ground) in the main campus of Chongqing University (29.57°N, 106.46°E) in the urban center of Chongqing, southwest China. The site is characterized by a typical residential and commercial environment, mainly influenced by local emissions (e.g., traffic, cooking). All instruments were installed in an air-conditioned room, with the room temperature maintained about 25°C. The ambient air was sampled at a flowrate of 16.7 LPM through a $PM_{2.5}$ impactor (model 2000-30EH, URG Inc.) and dried with a Nafion dryer (model MD-700, Perma Pure LLC), to achieve a low relative humidity level (RH <35%) prior to the online aerosol size distribution, optical and hygroscopic measurements. During the observation period, urban Chongqing suffered a rare heatwave. The mean temperature and relative humidity during the study period and the same period from 2011 to 2021 in urban Chongqing are given in Figure S1. Based on the method proposed by Nairn and Fawcett (2014), the Excess Heat Factor (EHF) metric was accordingly calculated for this study (Figure S2a).

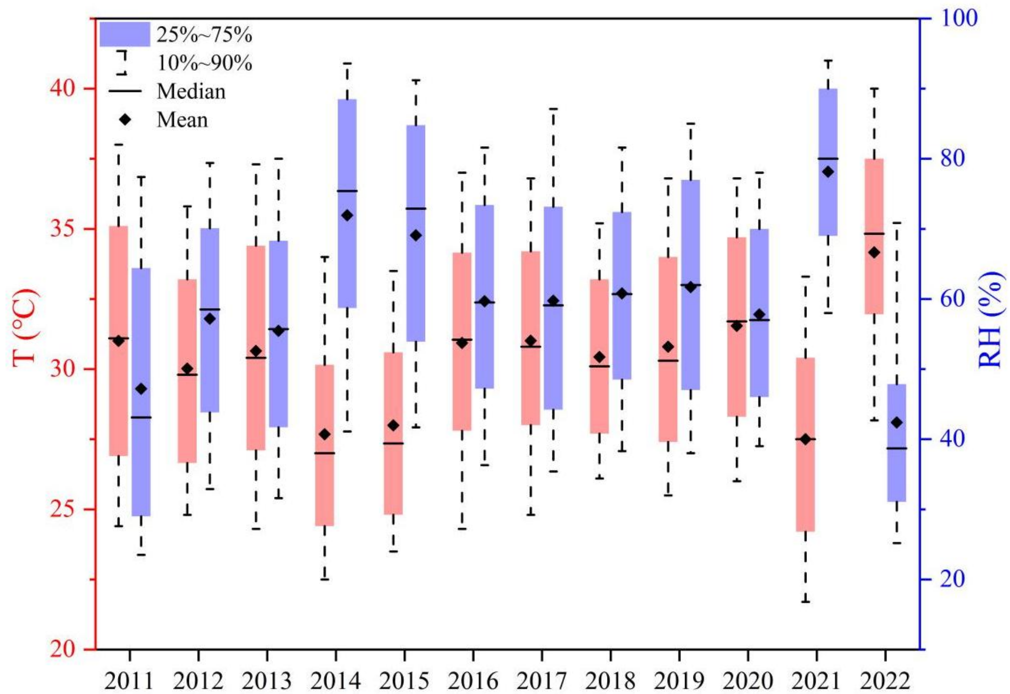

Figure S1. The variation trends of annual temperature and RH during the study period in 2022 and the same period from 2011 to 2021 in urban Chongqing.

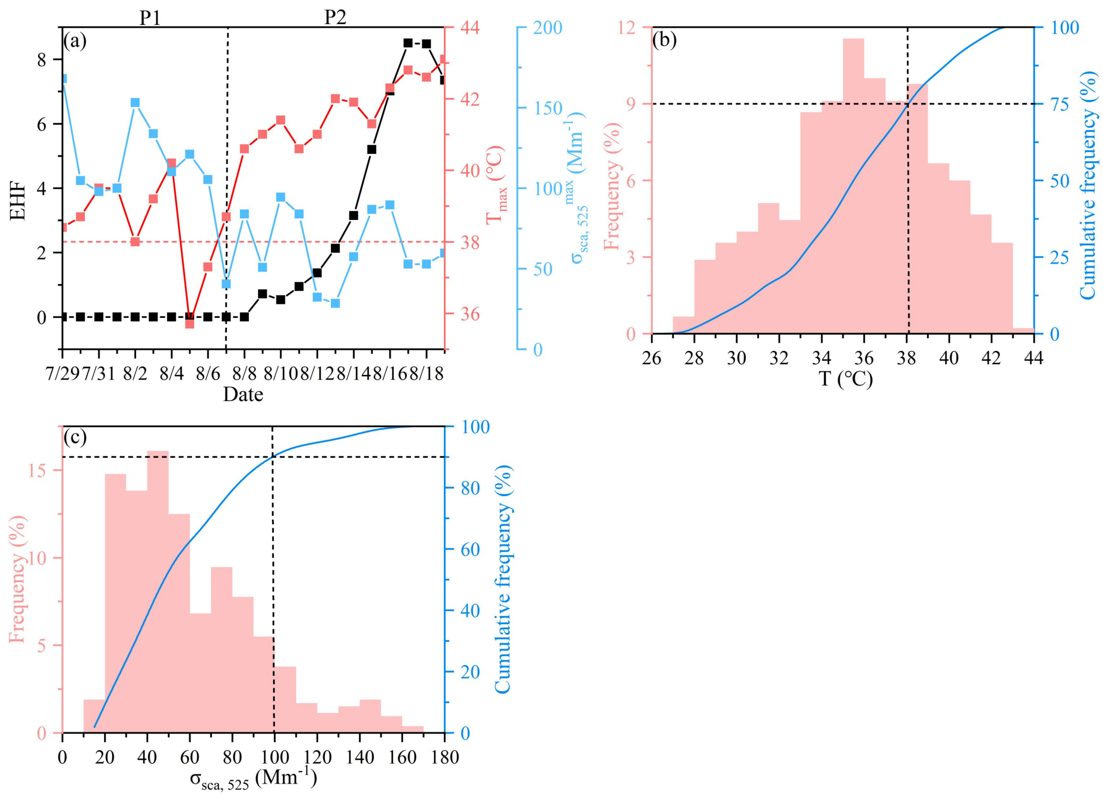

Figure S2. (a) Time series of calculated EHF, along with the daily maximum temperature (T_{max}) and dry $\sigma_{sca,\ 525}$ results, during the study period. The corresponding occurrence frequency and cumulative frequency of hourly **(b)** temperature and **(c)** $\sigma_{sca,\ 525}$ data records.

S2. Derivation of aerosol liquid water content (ALWC)

In this study, ALWC was determined as the discrepancy in aerosol volume concentration between the humidified and dry particles:

$$ALWC = V_{dry} \times (f_V(RH) - 1) \quad (1)$$

where the dry aerosol volume concentration (V_{dry}) was estimated with the dry scattering coefficients at three wavelengths utilizing a machine learning method (Kuang et al., 2018). Given the dependence on aerosol hygroscopicity and size distribution, the aerosol volume growth factor ($f_V(RH)$) can be obtained from the observed $f(RH)$ and SAE (a proxy of aerosol size distribution) with the humidified nephelometer system (Kuang et al., 2018). Accordingly, the fraction of aerosol water content (f_W) upon hydration could be expressed as:

$$f_W = \frac{ALWC}{ALWC + V_{dry}} \quad (2)$$

Both dry and humidified nephelometers were calibrated before the measurement for the zero/span check with the particle-free air/standard gas (R134a), following standard calibration procedures. More detailed descriptions about the home-built humidified nephelometer system can refer to Kuang et al. (2017, 2020) and Xue et al. (2022).

S3. Offline particle sampling and chemical analysis

Total suspended particle (TSP) filter samples were collected by a moderate volume air sampler at a flow rate of 200 L/min from August 5 to 19, 2022. Daily (from 9:30 a.m. to 9:00 a.m. of the next day) integrated ambient TSP samples were collected on prebaked (600℃, 5h) quartz-fiber filters (90 mm, Whatman) for water-soluble ions, organic carbon (OC), and elemental carbon (EC) analysis.

Water-soluble inorganic anions (i.e., SO_4^{2-}, NO_3^-, Cl^- and F^-) and cations (i.e., NH_4^+, Na^+, Mg^{2+}, $Ca^{2+}$and K^+) were quantified using an ion chromatograph analyzer (Dionex 600, Dionex, USA) following standard procedures (Peng et al., 2019; Wang et al., 2018). Elemental carbon (EC) and organic carbon (OC) in the collected TSP samples were analyzed using a DRI Model 2015 Multi-wavelength Carbon Analyzer (Magee Scientific, USA). The methodology for OC/EC analysis was based on the thermal-optical reflectance (TOR) method following the Interagency Monitoring of Protected Visual Environments (IMPROVE-A) protocol, as shown in Chow et al. (2007, 2011) and Peng et al. (2020). The secondary organic carbon (SOC) can be estimated with the obtained OC and EC data according to the EC-tracer method (Castro et al., 1999; Strader et al., 1999), details of which was also available in our previous study (Hao et al., 2024).

The chemical components mass concentration and mass fraction in TSP, as well as the $PM_{2.5}$ (PM_{10}) mass concentration and the ratio of SOC/TOC during the study period are depicted in Figure S3.

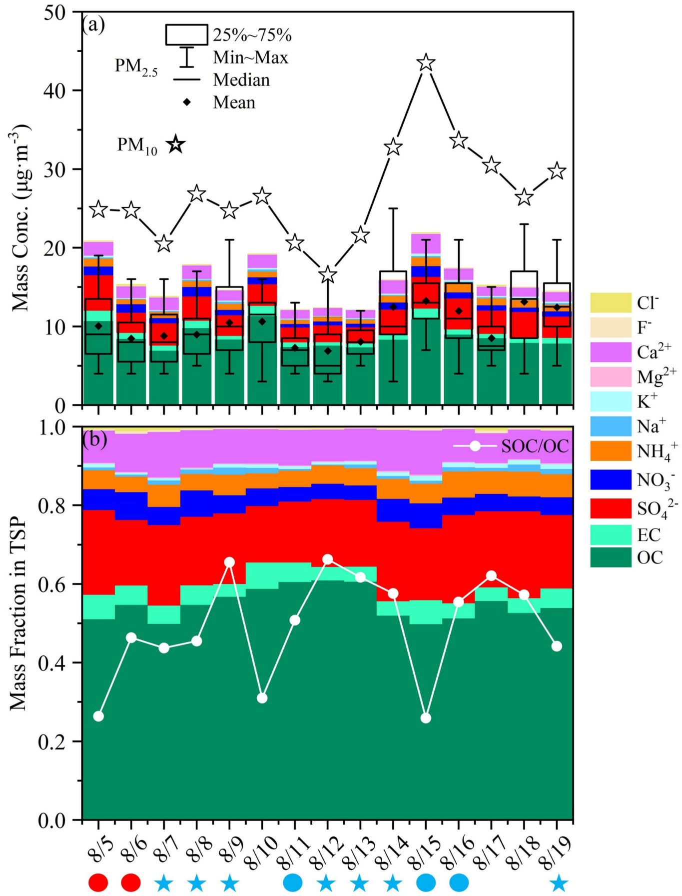

Figure S3. The mass concentration **(a)** and mass fraction **(b)** of chemical components in TSP (total suspended particulates) during the study period. The black stars, box plots and white line stands for daily mean PM_{10}, $PM_{2.5}$ and SOC/OC, respectively. The red or blue circle symbols below specific dates represent the P1 or P2 non-event days, and the blue stars represent the P2 $NPF_{clean, HW}$ days.

S4. Meteorological and air quality data

All the contemporary hourly meteorological datasets including relative humidity (RH), temperature (T), visibility (VIS), wind speed (WS), wind direction (WD), precipitation were obtained from the Integrated Surface Database from the U.S. National Centers for Environmental Information (https://ncdc.noaa.gov/isd) (Wan et al., 2023; Xu et al., 2020), and the mixing layer height (MLH) data were achieved from China Meteorological Administration in this study. Ultraviolet (UV) radiation data were downloaded from European Centre for Medium-Range Weather Forecasts (https://cds.climate.copernicus.eu/).

Hourly air pollutant datasets including $PM_{2.5}$, PM_{10}, NO_2, SO_2, CO and O_3 were achieved from the China National Environmental Monitoring Center (http://www.cnemc.cn/en). The gas-phase sulfuric acid, known as the most ubiquitous and key precursor for NPF, was estimated with the UVB (UVB = 5%UV, Fitsiou et al., 2021) and SO_2 concentration (Lu et al., 2019):

$$H_2SO_4 = 280.05 \times UVB^{0.14} \times SO_2{}^{0.40} \quad (3)$$

S5. Particle number size distribution measurements

During the field observation, every 3-min PNSD and particle volume size distribution (PVSD) was measured by a SMPS, which consisted of a soft X-Ray neutralizer (model 3088, TSI Inc.), a differential mobility analyzer (model 3081, TSI Inc.), and a condensation particle counter (model 3775, TSI Inc.) (Dominick et al., 2018; Rissler et al., 2006). The SMPS was operated at a sheath/sample flow rate of 3.0/0.3 LPM, and the detected size range was 14.1-710.5 nm with 110 size bins. Data inversion of measured particle size distributions was achieved with the Aerosol Instrument Manager software (AIM, TSI Inc.), including the multiple charge and diffusion corrections (Denjean et al., 2015; Rosati et al., 2022).

The aerosol effective radius (R_{eff}) is a crucial parameter regulating optical properties (e.g., light scattering) of the aerosol population (Hansen and Travis, 1974; Grainger et al., 1995). It can be calculated with the measured size distribution as below (Hansen and Travis, 1974; Grainger et al., 1995):

$$R_{eff} = \frac{\int D_P{}^3 n(\log D_P)\, d\log D_P}{\int D_P{}^2 n(\log D_P)\, d\log D_P} \quad (4)$$

where $n(\log D_P)$ is the particle number size distribution in log scale.

Using the measured PNSD data, NPF events were identified according to the criteria raised by Dal Maso et al. (2005), and the key parameters related to NPF events (e.g., formation rate (FR) and growth rate (GR) of new particles, condensation sink (CS) and coagulation sink (CoagS)) could be derived following the methodologies introduced by Dal Maso et al. (2005) and Kulmala et al. (2012).

The specific dates for NPF and non-event classifications were summarized in Table S1, and the frequencies of NPF, non-event and Undefined days during both periods were shown in Figure S4a. By using the HYSPLIT (Hybrid Single-Particle Lagrangian Integrated Trajectory) 4 model developed by NOAA (Stein et al., 2015), the 48-h and 72-h back trajectories of air masses at 500 or 1000 m altitude above the observation site during this study period were calculated and visualized by MeteoInfoMap (version 3.9.9; Figure S4b) (Chen et al., 2021; Tian et al., 2021; Wang, 2014).

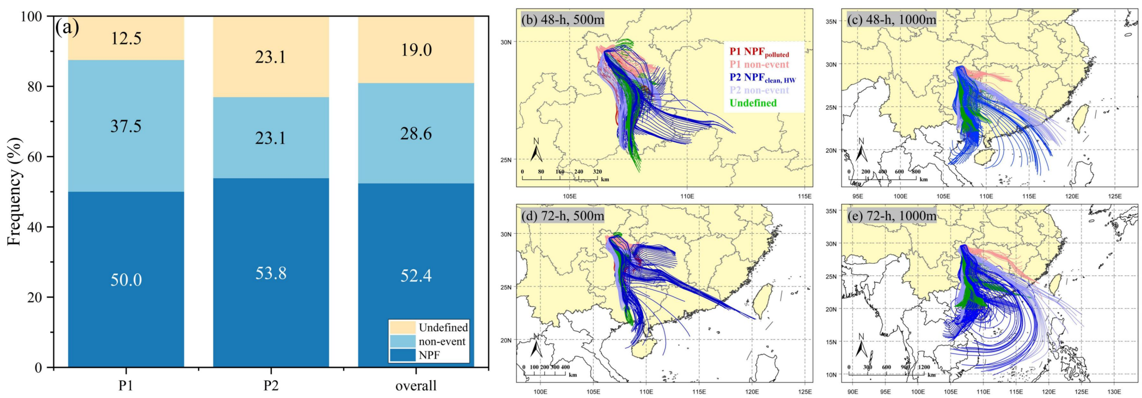

Figure S4. (a) The occurrence frequencies of NPF, non-event and Undefined days during P1, P2 and the whole observation periods. **(b-e)** The 48-h and 72-h air-mass back trajectories at 500 or 1000 m altitude during the study period.

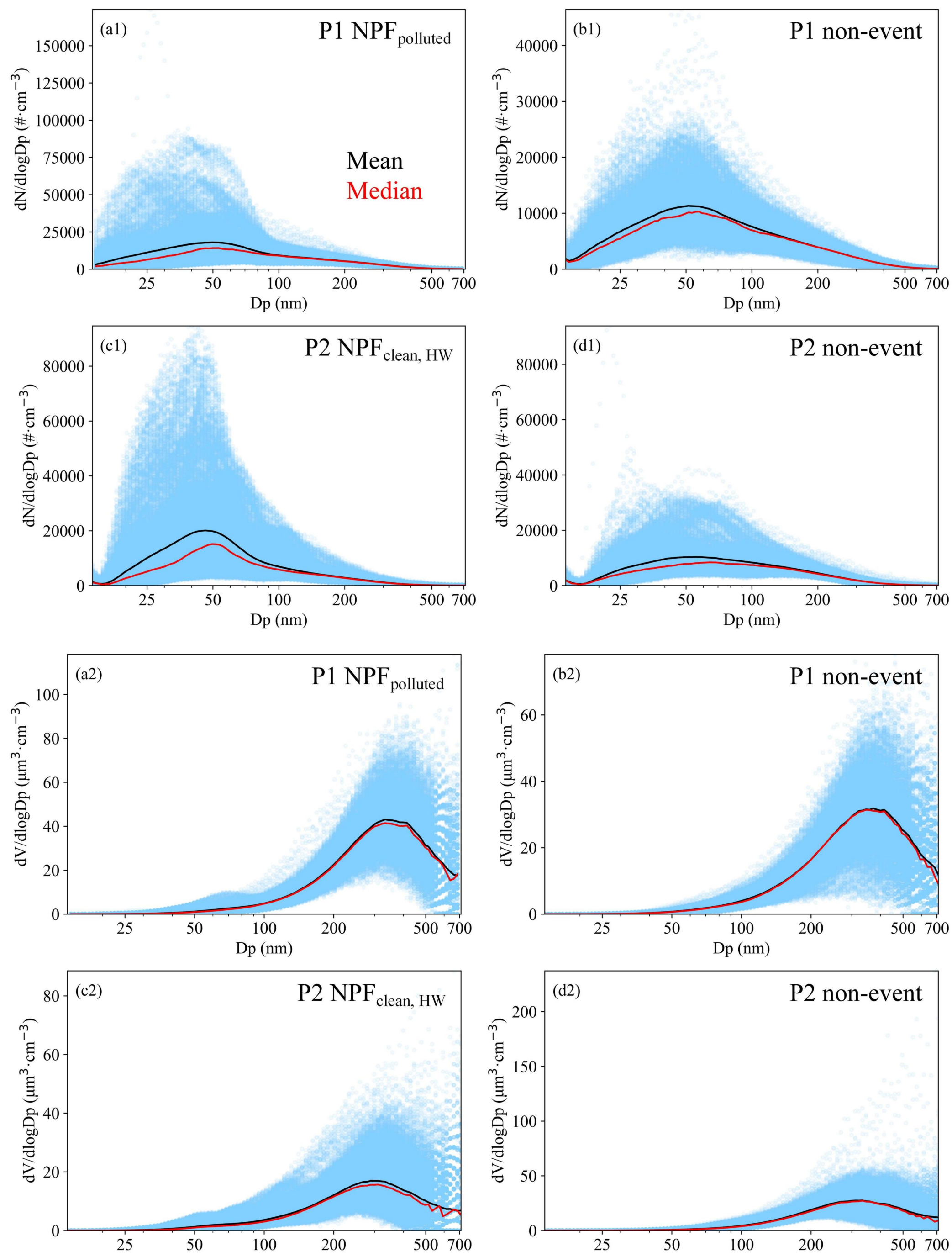

Figure S5. The PNSDs **(a1-d1)** and PVSDs **(a2-d2)** for different event categories. The black and red lines represent the mean and median values, respectively.

The diurnal variations of PNSD, R_{eff}, particle mode diameter (D_{mode}), as well as CS, were given in Figure S6.

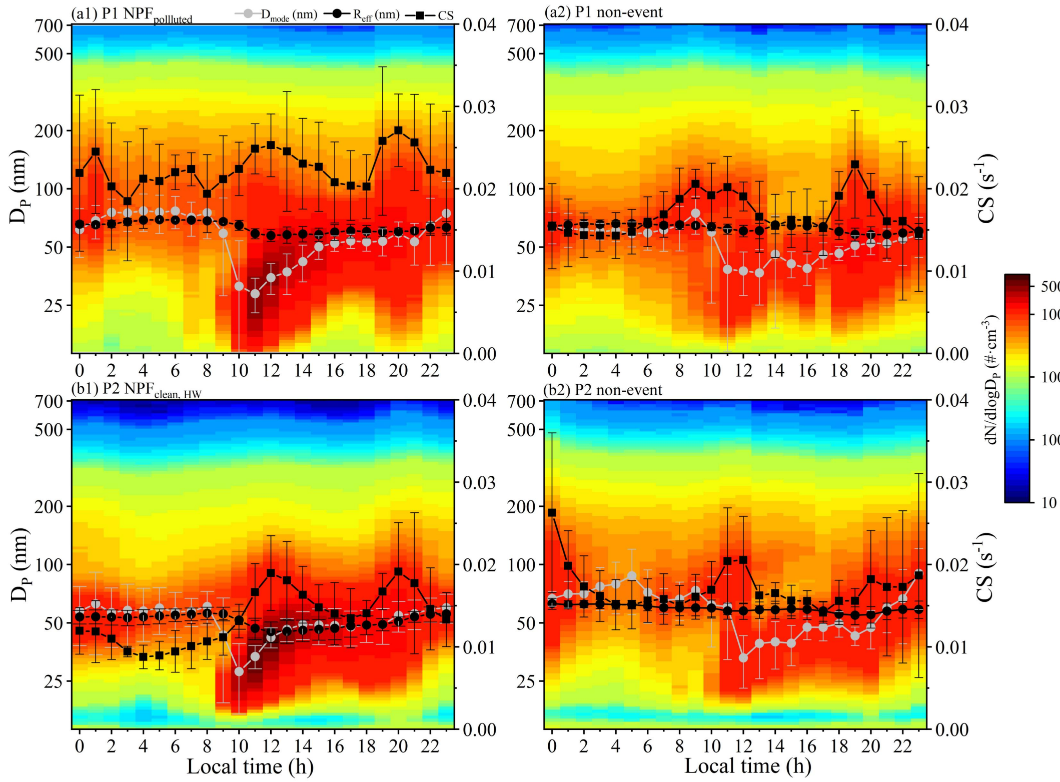

Figure S6. Diurnal variations of PNSDs, D_{mode}, R_{eff}, and CS during P1 and P2 NPF days **(a1, b1)** and non-event days **(a2, b2)**, the error bars stand for ± one standard deviations.

The PNSD is typically categorized into three modes: the nucleation mode (D_p <25 nm), Aitken mode (25-100 nm), and accumulation mode (D_p >100 nm) (Zhu et al., 2021). The number and volume concentrations of different mode particles for the corresponding NPF and non-event days during both P1 and P2 periods are shown in Figure S7. The diurnal variations of aerosol number and volume concentrations, as well as R_{eff}, for different modes on NPF event days are illustrated in Figure S8.

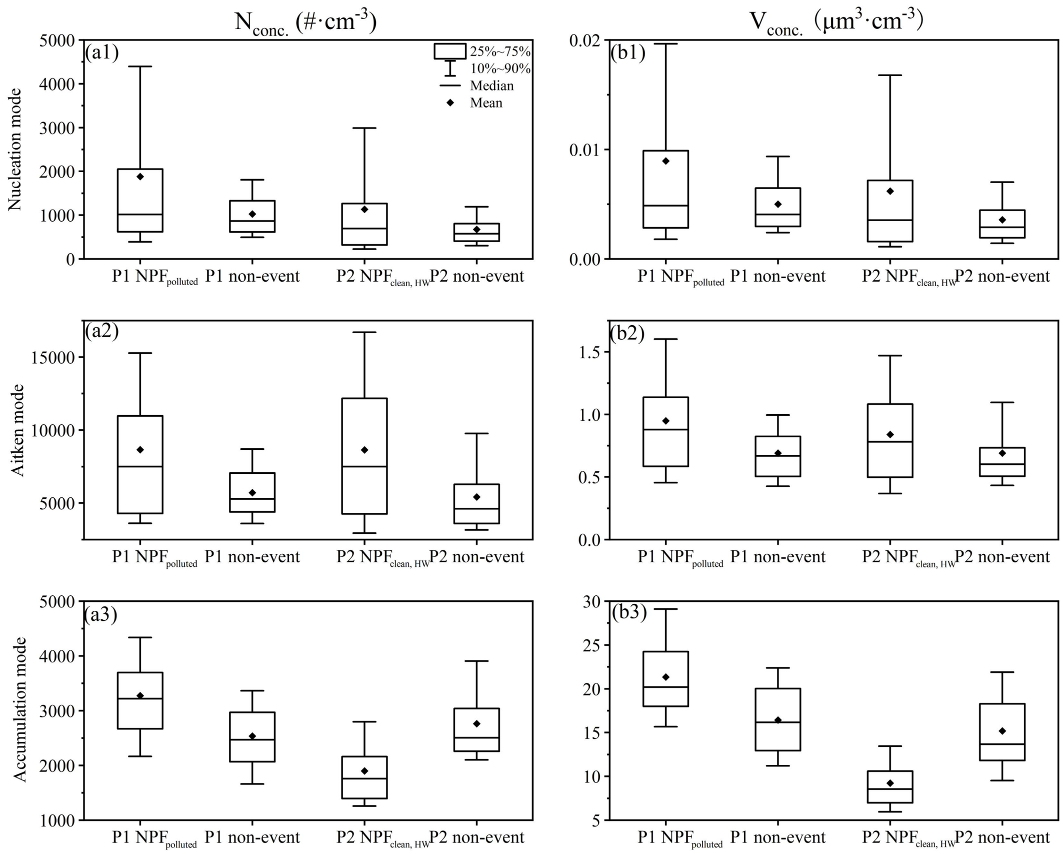

Figure S7. The number concentrations (left column: a1-a3) and volume concentrations (right column: b1-b3) of different mode particles for the corresponding NPF and non-event days during both P1 and P2 periods.

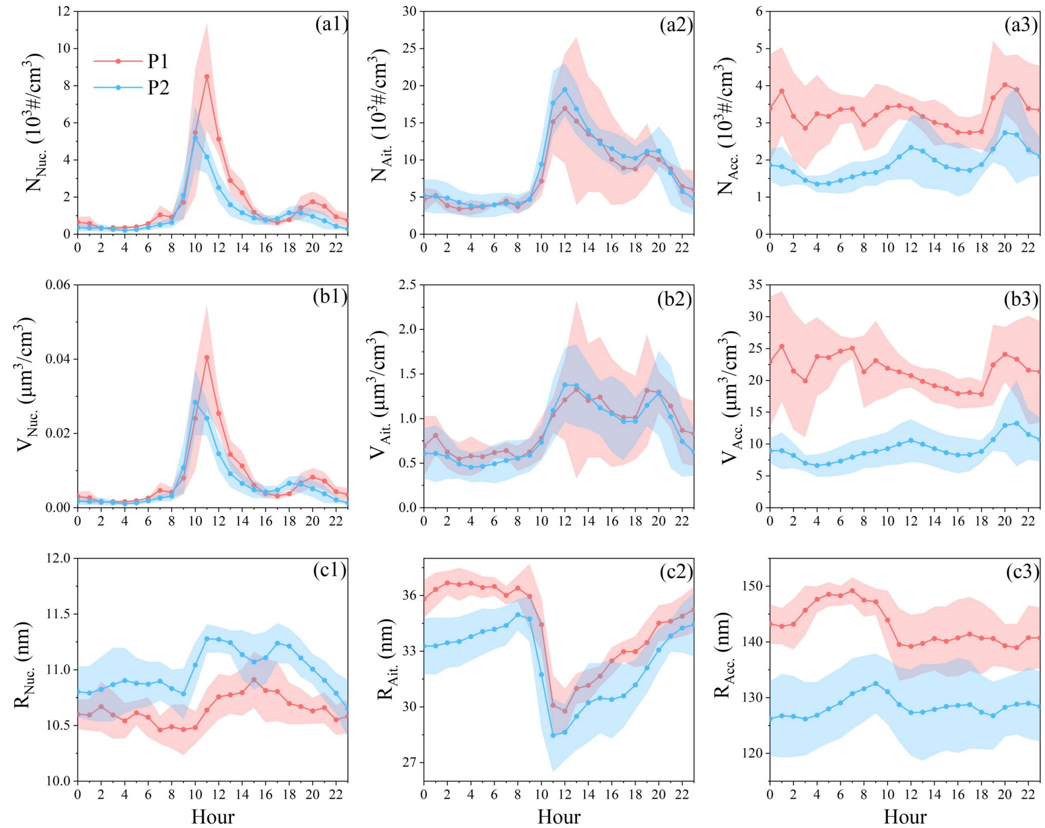

Figure S8. Diurnal variations of the number (**a1-a3**), volume (**b1-b3**) concentration and effective radius (**c1-c3**) of nucleation mode (left column), Aitken mode (middle column), and accumulation mode (right column) particles on NPF event days during P1 (red line) and P2 (blue line) periods. The shaded areas stand for the corresponding ± 1σ standard deviations.

The specific start and end time of NPF, along with the subsequent growth end time during NPF events were displayed in Figure S9. The NPF event end time is defined as the moment when the formation of new nucleation-mode particles (diameter <25 nm) ceases, specifically identified by the absence of a notable increase in sub-25 nm particles (Dal Maso et al., 2005; Hamed et al., 2007; Kerminen et al., 2018). The growth event end time refers to the time when the newly formed particles stop growing, typically due to the depletion of low-volatility vapors or particle coagulation (Dal Maso et al., 2005; Kerminen et al., 2018). This can be observed as the stabilization of particle diameters in the Aitken/accumulation mode, marked by a flattening of the growth trajectory in the PNSD plot (Figure 1i).

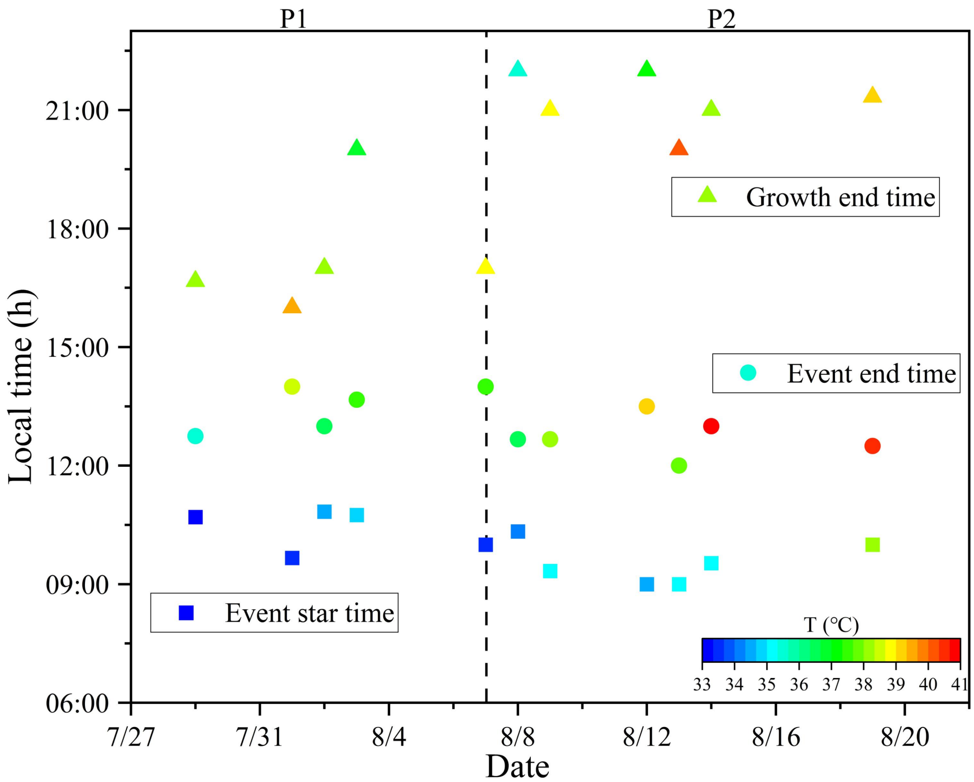

Figure S9. The start and end time of NPF, along with the subsequent growth end time and their corresponding temperature levels during NPF events.

S6. Diurnal variations of humidified nephelometer system related parameters on non-event days during both P1 and P2 periods

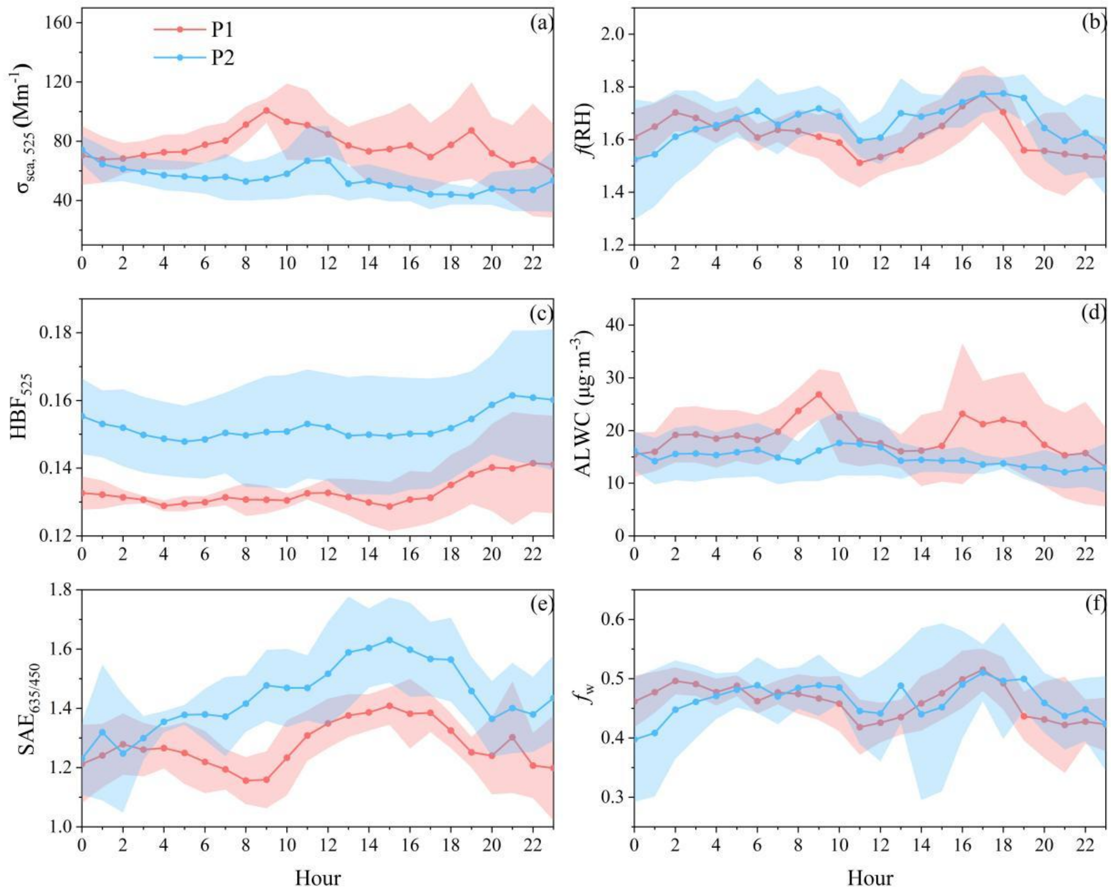

Figure S10. Diurnal variations of $\sigma_{sca,\ 525}$ **(a)**, f(RH) **(b)**, HBF_{525} **(c)**, ALWC **(d)**, $SAE_{635/450}$ **(e)** and f_W **(f)** on non-event days during P1 (red line) and P2 (blue line) periods. The shaded areas stand for the corresponding ± 1σ standard deviations.

S7. Calculation of σ_{sca} and HBF with the Mie theory and measured PNSD

The size-dependent efficiencies of σ_{sca}, σ_{bsca} and HBF in dry conditions, as well as the corresponding enhancements in these efficiencies of a single particle upon hydration at λ = 525 nm could be simulated using the Mie model. Aerosol diameter growth factor (g(RH)) is normally determined by the aerosol hygroscopicity parameter κ (Brock et al., 2016; Tan et al., 2024). The bulk aerosol $\kappa_{f\text{(RH)}}$ of this study could be derived from the *f*(RH) measurements based on the method proposed by Kuang et al. (2017). The aerosol population was typically divided into the ultrafine (D_p <100 nm; Uf.) and accumulation (D_p ≥100 nm; Acc.) modes (Fig. S5). Although the size-resolved κ results were unavailable, the mean κ_i for both Uf. and Acc. mode particles could be roughly estimated assuming that $\kappa_{f\text{(RH)}}$ is a linear combination of volume-weighted κ_i for different modes (Hong et al., 2024). Since the hygroscopicity for Uf. mode was generally weaker (Chen et al., 2012; Petters and Kreidenweis, 2007), the mean $\kappa_{\text{Uf.}}$ was defined to be half of the measured bulk $\kappa_{f\text{(RH)}}$, and $\kappa_{\text{Acc.}}$ can be derived from the bulk $\kappa_{f\text{(RH)}}$ with the measured $VF_{\text{Uf.}}$ and $VF_{\text{Acc.}}$. Consequently, the corresponding g(RH) for both Uf. and Acc. modes can be calculated with the κ-Köhler theory. The complex refractive index is another critical input parameter for the Mie model, with the real part of complex refractive index (*n*) determining the aerosol light scattering ability. Under the assumption of a fixed *n* for dry aerosols (n_{dry} = 1.53) in this study, the volume-weighted *n* of hydrated particles can be derived with n_{dry} and *f*(RH)-derived volume fractions of uptake water, f_W and the *n* of pure water (1.33; Jung et al., 2016) (Chen et al., 2012). Hence, the efficiencies of σ_{sca}, σ_{bsca} and HBF after hygroscopic growth could be simulated with the time-averaged dry PNSD, the mean g(RH) of Uf. Mode (1.15) and Acc. mode (1.27), and the mean *n* of humidified aerosols (1.44) for the observation period. The theoretically simulated results are displayed in Figure S11.

A good correlation between SMPS-determined particle volume concentration and the measured $\sigma_{sca,\ 525}$ is also observed in Figure S12. The size-resolved $\sigma_{sca,\ 525}$ distributions and size-resolved $\sigma_{sca,\ 525}$ cumulative frequency distribution on NPF event (non-event) days during P1 and P2 periods are displayed in Figure S13.

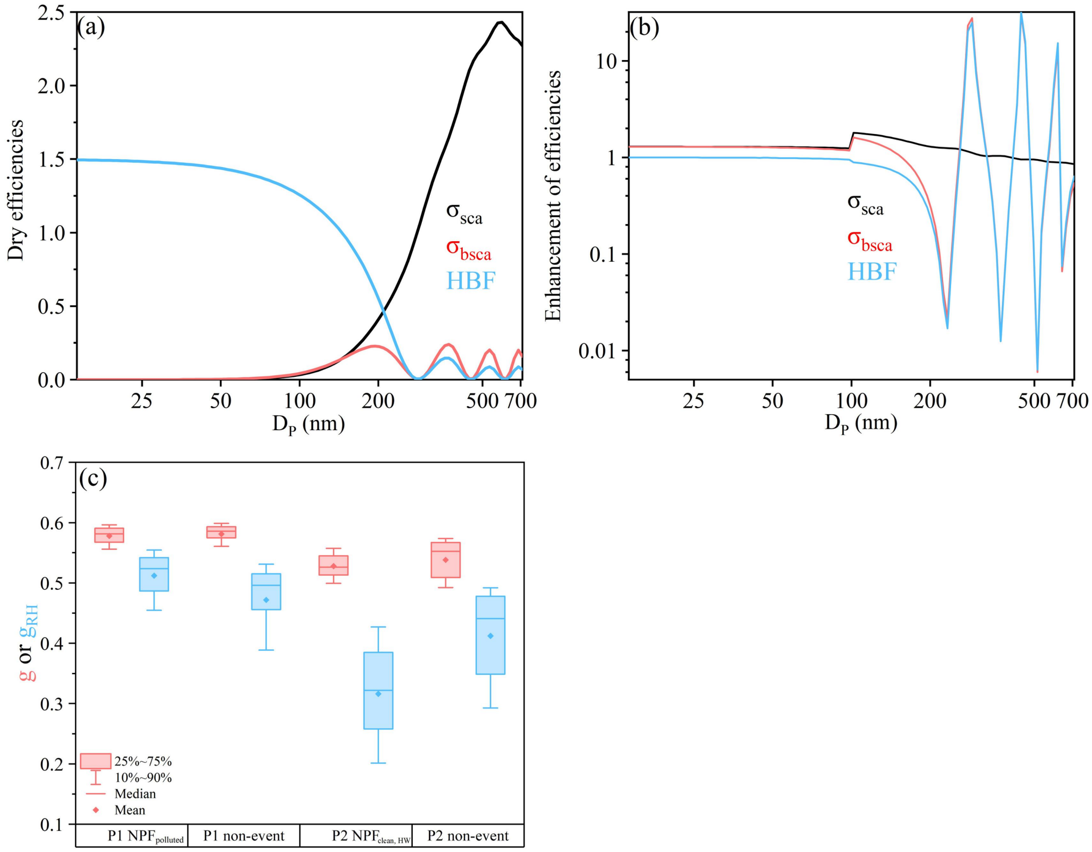

Figure S11. Size-dependent efficiencies of **(a)** light scattering (the black line), backscattering (the red line) and HBF (the blue line) in dry conditions, as well as **(b)** the enhancements in corresponding efficiencies of light scattering (the black line), backscattering (the red line) and HBF (the blue line) at λ = 525 nm simulated with the Mie theory. **(c)** The box plots of the HBF_{525} ($HBF_{525, RH}$) derived asymmetry factor g (g_{RH}).

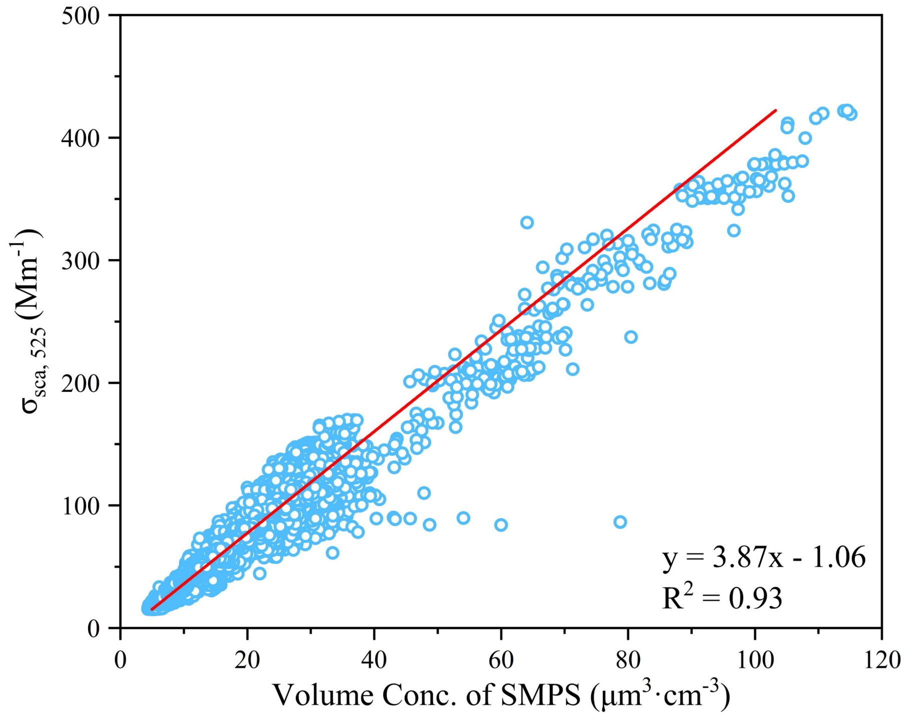

Figure S12. Correlation between the particle volume concentration determined by SMPS and $\sigma_{sca,\ 525}$ measured by the humidified nephelometer system during the study period. The solid line represents the fitting line.

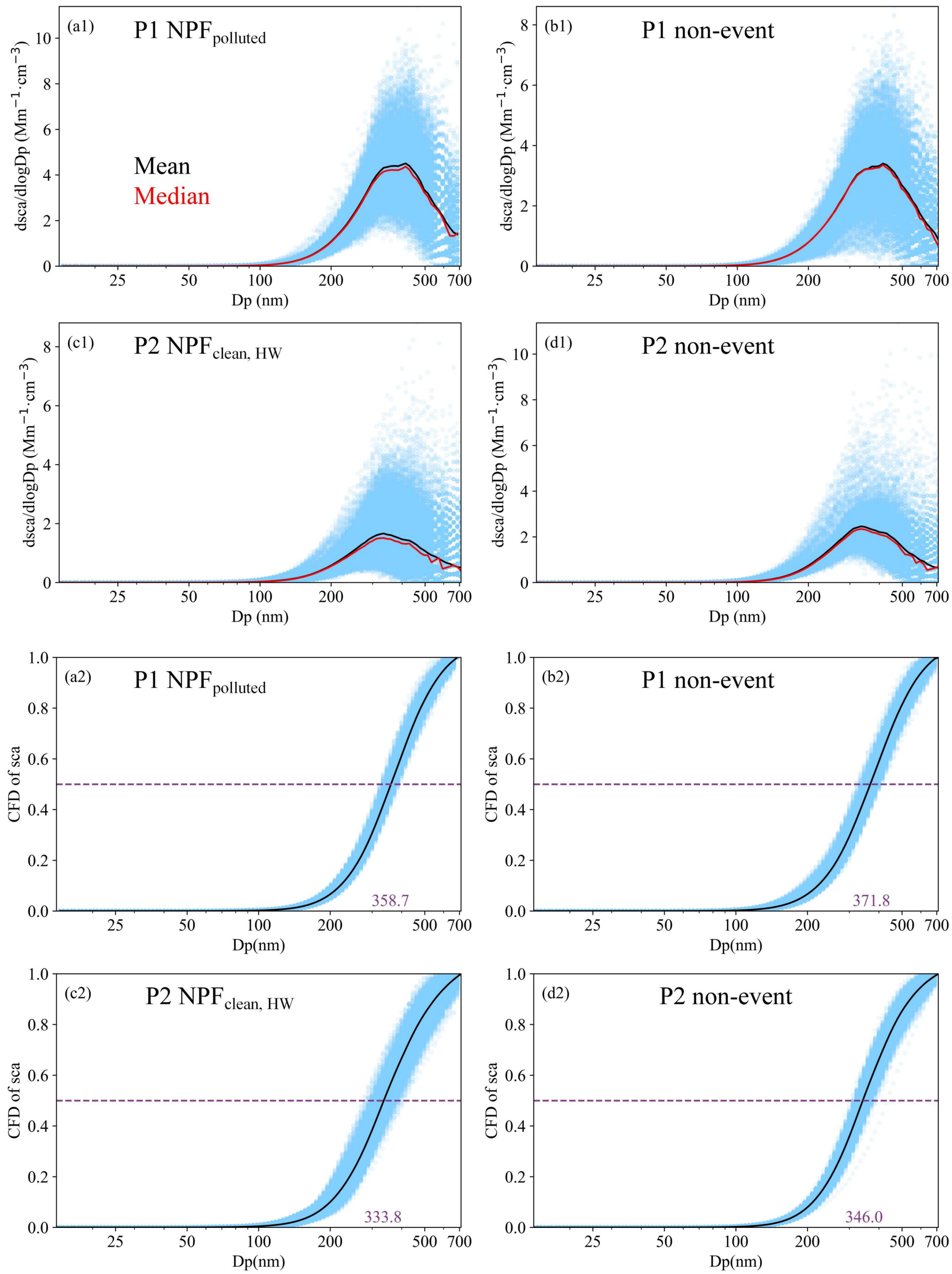

Figure S13. The size-resolved $\sigma_{sca,\ 525}$ distributions **(a1-d1)** and size-resolved $\sigma_{sca,\ 525}$ cumulative frequency distribution **(a2-d2)** for different event categories. The black and red lines represent the mean and median values, the purple dashed line and the purple numbers on the abscissa represent the 50% cumulative frequency and the corresponding particle size (D_{50}), respectively.

S8. Correlation coefficients between different PNSD-related parameters, temperature, O_3/O_X, aerosol optical and hygroscopic properties on NPF (non-event) days during either P1 or P2 period

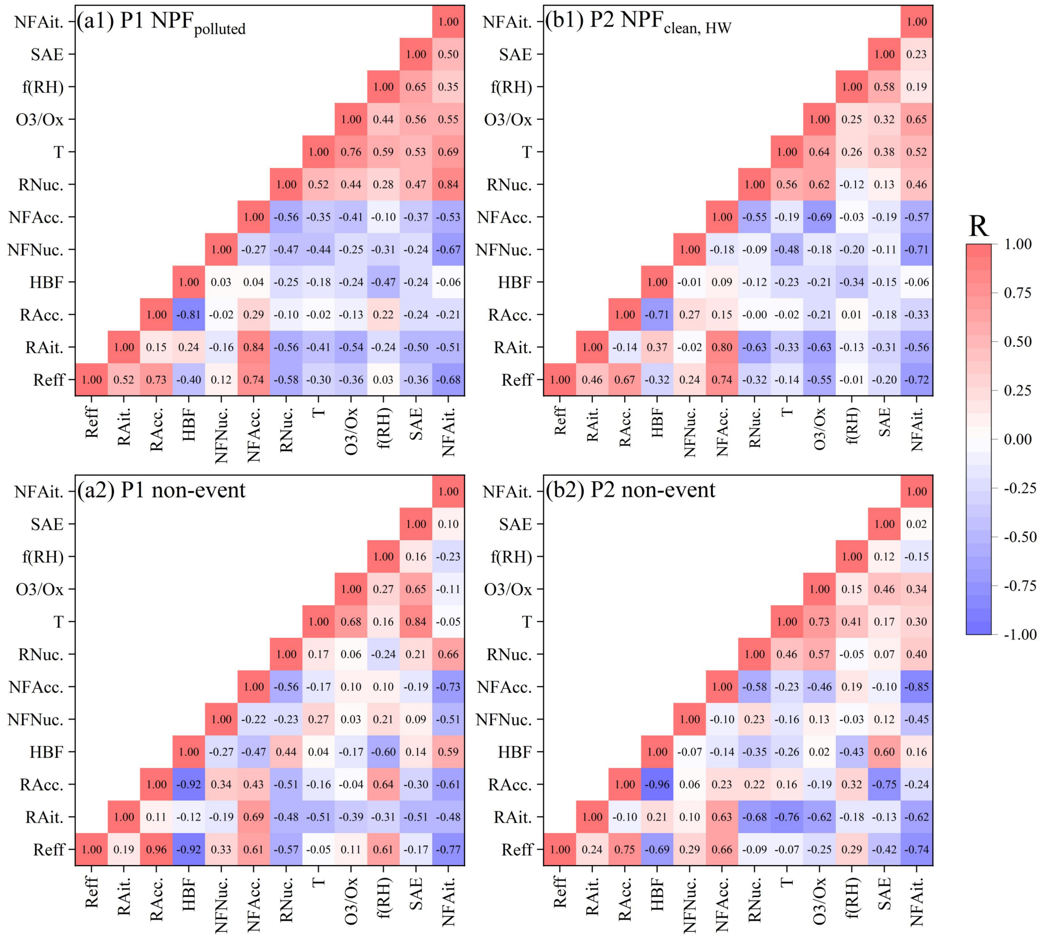

Figure S14. Correlation coefficients between different PNSD-related parameters (R_{eff}, $R_{Nuc.}$, $R_{Ait.}$, $R_{Acc.}$, $NF_{Nuc.}$, $NF_{Ait.}$, $NF_{Acc.}$), temperature (T), O_3/O_X, HBF, SAE, and *f*(RH) during NPF events **(a1, b1)** and non-event days **(a2, b2)** over the 08:00-22:00 LT time window.

S9.The sensitive test on dependences of the $HBF_{525,\,RH}/HBF_{525}$ ratio on the aerosol size distribution, hygroscopic growth, and complex refractive index

To investigate the distinct influences of PNSD, optical and hygroscopic properties on the $HBF_{525,\,RH}/HBF_{525}$ ratio, a sensitivity analysis with the measured data specifically for both P1 and P2 NPF days using the Mie model was conducted. Aerosol number size distributions could be assumed as a combination of multi-lognormal distribution functions, with each mode representing a distinct particle population (Hussein et al., 2004):

$$\frac{dN}{d\log D_P}=\sum_{i=1}^{n}\frac{N_{t,i}}{\sqrt{2\pi}\log\sigma_{g,i}}\exp\left[-\frac{(\log D_P-\log\overline{D_{Pg,i}})^2}{2\log^2\sigma_{g,i}}\right] \quad (5)$$

Where the three representative parameters, i.e., the total number concentration $N_{t,\,i}$, the geometric standard deviation (GSD) $\sigma_{g,\,i}$, and the geometrical mean diameter $D_{Pg,\,i}$, can be used to characterize an individual mode i; and n is the number of individual modes (Hussein et al., 2004). In this study, the measured PNSD data on NPF days during P1 and P2 periods were normally fitted into two modes: the predominant Uf. mode and the other one dominated by Acc. Mode particles (Fig. S5). The geometrical mean diameter of fitted ultrafine mode (GMD_{Uf}) from $NPF_{clean,\,HW}$ onset until 19:00 LT was shown in Figure S15.

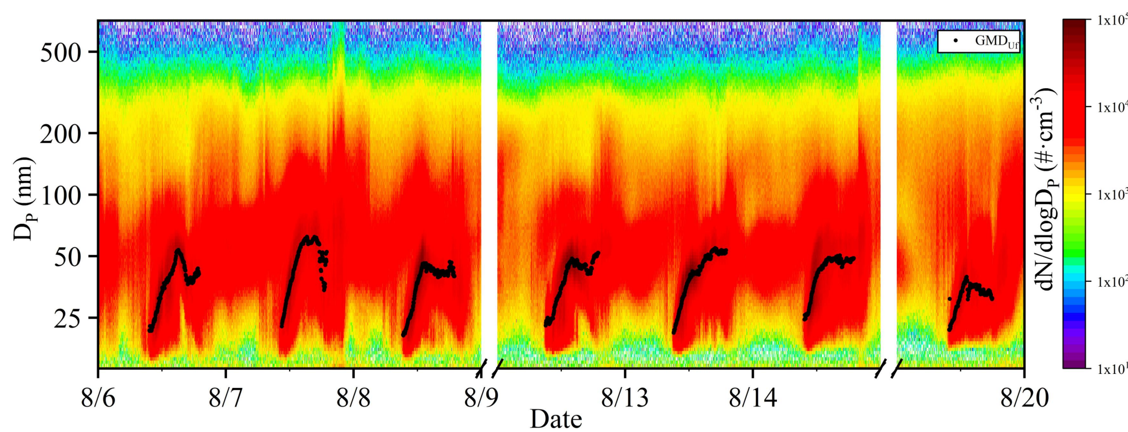

Figure S15. Overview of the measured PNSD and geometrical mean diameter of the fitted ultrafine mode (GMD_{Uf}; black dots) during the P2 $NPF_{clean,\,HW}$ days.

Hence, nine parameters were employed in the Mie model: four parameter pairs (D_{Pg}, GSD, N_t and g(RH)) for both Uf. and Acc. mode particles, along with the mean *n* of the bulk aerosol population upon hydration. Further, the $HBF_{525, RH}/HBF_{525}$ can be simplified as a function of aerosol size distribution (i.e., D_{Pg}, GSD, N_t), water uptake (e.g., g(RH)), and *n* as below:

$$HBF_{525, RH}/HBF_{525} = f(D_{Pg}, GSD, N_t, g(RH), n) \quad (6)$$

The influence of a specific parameter on the $HBF_{525, RH}/HBF_{525}$ was evaluated by fixing all the other parameters at their measured mean values and computing $HBF_{525, RH}/HBF_{525}$ ratios across the range of this target parameter.

The measured mean value and variation range of each parameter were summarized in Table S3. The ranges of D_{Pg}, GSD, N_t and g(RH) were determined based on field measurements of this study. Zhao et al. (2021) reported that *n* of diverse aerosol populations could range from 1.36 to 1.78 across different Chinese cities, and this study constrained *n* to vary from 1.3 (nearly pure water of 1.33; Jung et al., 2016) to 1.8 (similar to black carbon of approximately 1.87; Schkolnik et al., 2007) in the modeling framework. The results are shown in Figures S16-17.

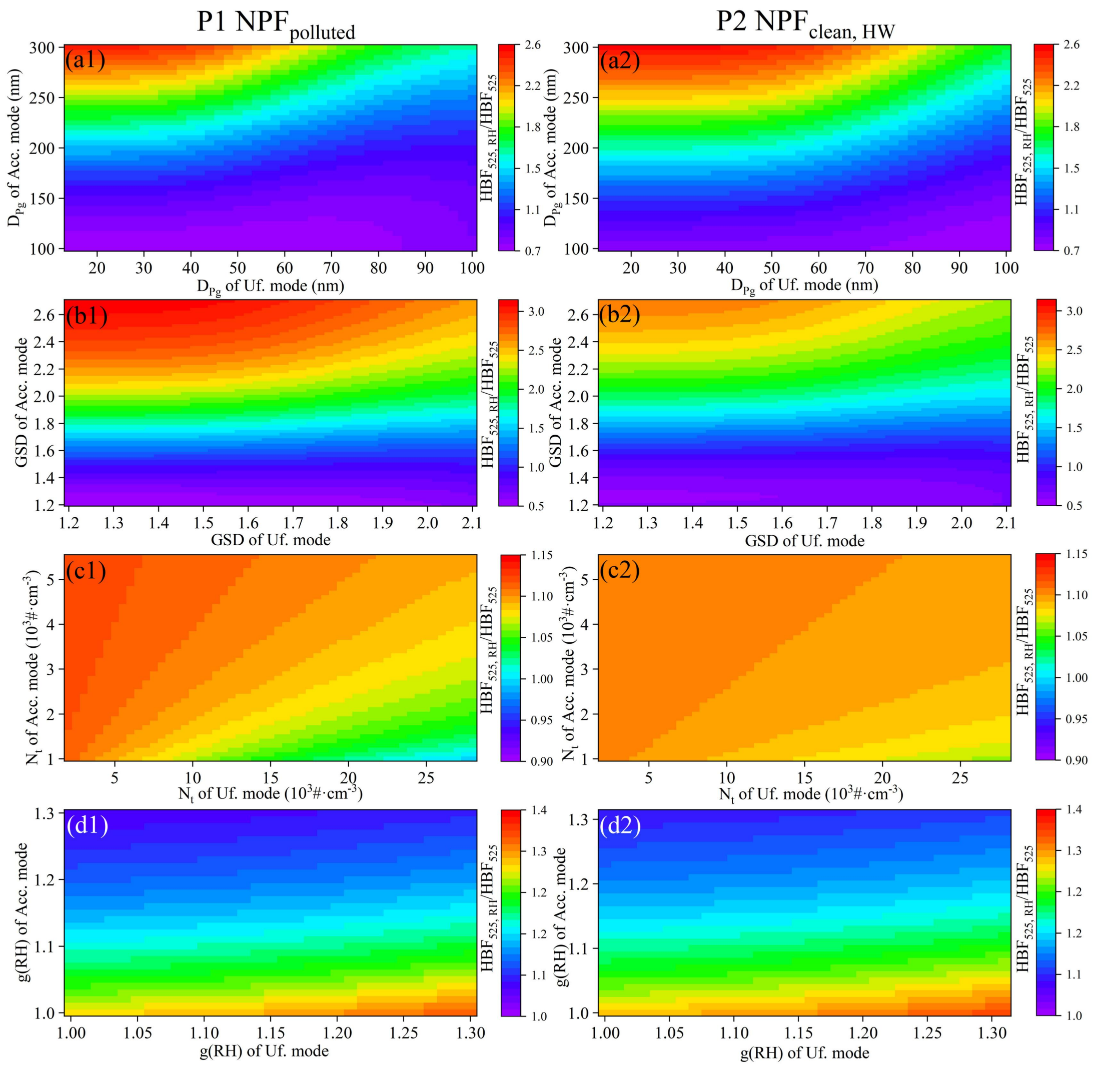

Figure S16. The relationships between the $HBF_{525, RH}/HBF_{525}$ ratios and the D_{pg} **(a)**, GSD **(b)**, N_t **(c)**, g(RH) **(d)** of two modes particleas. The left (right) column was corresponding to the P1 NPF$_{polluted}$ (P2 NPF$_{clean, HW}$) days.

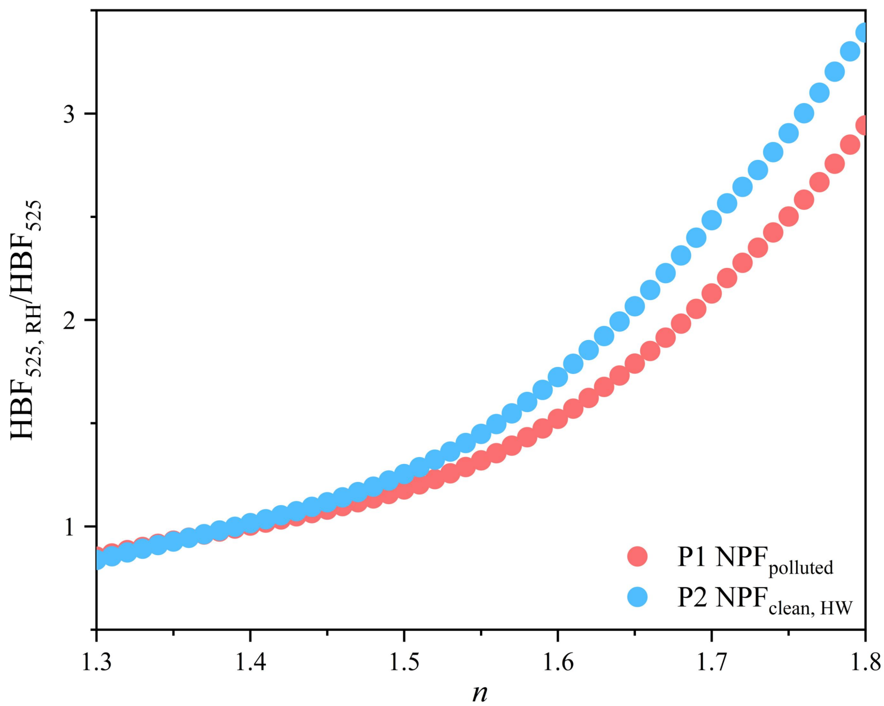

281

282 **Figure S17.** The variations of the $HBF_{525, RH}/HBF_{525}$ ratios with *n* on the P1 and P2 NPF

283 days.

Table S1. Specific dates for different event categories during P1 and P2 periods.

Period	Category	Date
P1	$NPF_{polluted}$	7.29, 8.1-3
	non-event	8.4-6
	Undefined	7.30-31
P2	$NPF_{clean,\ HW}$	8.7-9, 8.12-14, 8.19
	non-event	8.11, 8.15-16
	Undefined	8.10, 8.17-18

Table S2. A summary (avg. ± std.) of the humidified nephelometer system determined parameters ($\sigma_{sca,\ 525}$, f(RH), ALWC, HBF_{525}, $SAE_{634/450}$, f_W), SMPS-relevant parameters ($N_{conc.}$, $V_{conc.}$, R_{eff}, $NF_{Acc.}$, $VF_{Acc.}$), meteorological parameters (T, RH, WS, VIS, MLH), air pollutants ($PM_{2.5}$, NO_2, SO_2, O_3, CO, O_3/O_X), NPF events related parameters (FR, GR, CS, CoagS), $HBF_{525,\ RH}/HBF_{525}$ and f_{RF}(RH) on NPF event and non-event days, as well as overall mean results during P1 and P2 periods.

	NPF		non-event		Overall	
	P1	P2	P1	P2	P1	P2
$\sigma_{sca,\ 525}$ (Mm^{-1})	103.8 ± 30.4	33.2 ± 11.7	76.7 ± 23.5	54.7 ± 17.6	88.0 ± 29.3	41.2 ± 16.0
f(RH)	1.64 ± 0.10	1.71 ± 0.13	1.62 ± 0.10	1.66 ± 0.12	1.61 ± 0.12	1.71 ± 0.15
ALWC ($\mu g \cdot m^{-3}$)	25.9 ± 6.6	10.2 ± 3.2	18.9 ± 7.5	14.8 ± 4.5	21.4 ± 7.8	12.0 ± 3.9
HBF_{525}	0.134 ± 0.007	0.157 ± 0.011	0.133 ± 0.008	0.152 ± 0.016	0.135 ± 0.008	0.153 ± 0.012
$SAE_{635/450}$	1.31 ± 0.10	1.48 ± 0.13	1.27 ± 0.11	1.44 ± 0.16	1.29 ± 0.12	1.47 ± 0.16
f_W	0.47 ± 0.04	0.48 ± 0.05	0.46 ± 0.04	0.46 ± 0.06	0.46 ± 0.05	0.48 ± 0.05
$N_{conc.}$ ($10^4 \# \cdot cm^{-3}$)	1.4 ± 0.7	1.2 ± 0.6	0.9 ± 0.3	0.9 ± 0.3	1.2 ± 0.6	1.0 ± 0.6
$V_{conc.}$ ($\mu m^3 \cdot cm^{-3}$)	22.5 ± 5.5	10.1 ± 3.6	17.0 ± 4.8	15.9 ± 5.6	19.5 ± 6.0	12.1 ± 5.0
R_{eff} (nm)	124.8 ± 10.7	102.8 ± 12.4	126.2 ± 10.6	118.6 ± 11.4	125.0 ± 10.0	110.6 ± 13.7
$NF_{ACC.}$	0.28 ± 0.11	0.20 ± 0.10	0.28 ± 0.06	0.33 ± 0.07	0.28 ± 0.09	0.26 ± 0.11
$VF_{ACC.}$	0.96 ± 0.02	0.91 ± 0.04	0.96 ± 0.02	0.96 ± 0.02	0.96 ± 0.02	0.93 ± 0.04
T (℃)	34.0 ± 3.4	36.8 ± 3.1	33.2 ± 3.3	37.6 ± 2.7	33.8 ± 3.4	37.3 ± 3.0
RH (%)	46.6 ± 14.1	34.7 ± 9.1	52.6 ± 13.0	34.0 ± 7.5	47.9 ± 13.7	33.5 ± 8.5
WS (m/s)	1.1 ± 0.6	1.8 ± 1.0	1.4 ± 1.1	1.6 ± 0.9	1.2 ± 0.8	1.8 ± 1.0
VIS (km)	23.3 ± 6.3	29.9 ± 0.7	25.7 ± 5.1	29.2 ± 2.1	25.0 ± 5.6	29.8 ± 1.2
MLH (m)	1062.0 ± 475.6	1461.3 ± 529.9	1075.6 ± 415.4	1340.8 ± 589.8	1063.3 ± 465.8	1454.8 ± 562.6
$PM_{2.5}$ ($\mu g \cdot m^{-3}$)	18.3 ± 6.2	9.3 ± 4.5	10.5 ± 4.2	11.8 ± 4.0	15.1 ± 6.6	10.1 ± 4.4
NO_2 ($\mu g \cdot m^{-3}$)	30.8 ± 18.7	22.7 ± 12.8	21.7 ± 9.6	33.4 ± 19.2	29.8 ± 19.1	24.8 ± 15.4
SO_2 ($\mu g \cdot m^{-3}$)	7.2 ± 1.8	8.8 ± 2.3	6.4 ± 1.5	9.6 ± 3.9	6.9 ± 1.8	9.0 ± 3.0
O_3 ($\mu g \cdot m^{-3}$)	108.2 ± 62.2	84.1 ± 50.2	98.7 ± 51.9	82.3 ± 58.3	100.2 ± 61.1	82.5 ± 49.5
CO ($mg \cdot m^{-3}$)	0.57 ± 0.10	0.44 ± 0.09	0.53 ± 0.05	0.51 ± 0.10	0.55 ± 0.10	0.45 ± 0.09
O_3/O_X	0.71 ± 0.24	0.72 ± 0.21	0.78 ± 0.14	0.62 ± 0.27	0.70 ± 0.25	0.70 ± 0.22
FR ($cm^{-3} \cdot s^{-1}$)	17.10 ± 7.79	11.22 ± 6.81	/	/	/	/
$GR_{<25\ nm}$ ($nm \cdot h^{-1}$)	13.68 ± 3.39	9.31 ± 3.23	/	/	/	/
$GR_{25\text{-}40\ nm}$ ($nm \cdot h^{-1}$)	7.12 ± 2.05	9.22 ± 4.28	/	/	/	/
$GR_{40\text{-}60\ nm}$ ($nm \cdot h^{-1}$)	6.87 ± 6.27	4.41 ± 1.72	/	/	/	/
$GR_{60\text{-}80\ nm}$ ($nm \cdot h^{-1}$)	10.73 ± 8.37	5.51 ± 2.98	/	/	/	/
CS (s^{-1})	2.3 ±	1.3 ±	/	/	/	/

	0.4×10^{-2}	0.3×10^{-2}				
CoagS (s^{-1})	$1.3 \pm 0.2\times10^{-4}$	$0.9 \pm 0.2\times10^{-4}$	/	/	/	/
$HBF_{525, RH}/HBF_{525}$	1.22 ± 0.10	1.78 ± 0.29	1.39 ± 0.24	1.43 ± 0.18	1.32 ± 0.19	1.63 ± 0.29
f_{RF}(RH)	1.89 ± 0.17	2.21 ± 0.23	1.93 ± 0.14	2.01 ± 0.18	1.91 ± 0.16	2.15 ± 0.23

Table S3. A summary of the input parameters for the sensitivity analysis with the Mie models.

	Variable	Mode	Mean	Range
P1 $NPF_{polluted}$	D_{Pg} (nm)	Uf.	39	14-100
		Acc.	173	100-300
	GSD	Uf.	1.69	1.2-2.1
		Acc.	1.56	1.2-2.7
	N_t ($\#\cdot cm^{-3}$)	Uf.	16,844	2,000-28,000
		Acc.	2,311	1,000-5,500
	g(RH)	Uf.	1.14	1.0-1.3
		Acc.	1.26	1.0-1.3
	n	/	1.45	1.3-1.8
P2 $NPF_{clean, HW}$	D_{Pg} (nm)	Uf.	39	14-100
		Acc.	150	100-300
	GSD	Uf.	1.46	1.2-2.1
		Acc.	1.65	1.2-2.7
	N_t ($\#\cdot cm^{-3}$)	Uf.	14,963	2,000-28,000
		Acc.	2,251	1,000-5,500
	g(RH)	Uf.	1.15	1.0-1.3
		Acc.	1.27	1.0-1.3
	n	/	1.44	1.3-1.8

References

Brock, C. A., Wagner, N. L., Anderson, B. E., Attwood, A. R., Beyersdorf, A., Campuzano-Jost, P., Carlton, A. G., Day, D. A., Diskin, G. S., Gordon, T. D., Jimenez, J. L., Lack, D. A., Liao, J., Markovic, M. Z., Middlebrook, A. M., Ng, N. L., Perring, A. E., Richardson, M. S., Schwarz, J. P., Washenfelder, R. A., Welti, A., Xu, L., Ziemba, L. D., and Murphy, D. M.: Aerosol optical properties in the southeastern United States in summer - Part 1: Hygroscopic growth, Atmos. Chem. Phys., 16, 4987–5007, https://doi.org/10.5194/acp-16-4987-2016, 2016.

Castro, L. M., Pio, C. A., Harrison, R. M., and Smith, D. J. T.: Carbonaceous aerosol in urban and rural European atmospheres: Estimation of secondary organic carbon concentrations, Atmos. Environ., 33, 2771–2781, https://doi.org/10.1016/S1352-2310(98)00331-8, 1999.

Chen, J., Wu, Z., Chen, J., Reicher, N., Fang, X., Rudich, Y., and Hu, M.: Size-resolved atmospheric ice-nucleating particles during East Asian dust events, Atmos. Chem. Phys., 21, 3491–3506, https://doi.org/10.5194/acp-21-3491-2021, 2021.

Chen, J., Zhao, C. S., Ma, N., Liu, P. F., Göbel, T., Hallbauer, E., Deng, Z. Z., Ran, L., Xu, W. Y., Liang, Z., Liu, H. J., Yan, P., Zhou, X. J., and Wiedensohler, A.: A parameterization of low visibilities for hazy days in the North China Plain, Atmos.

Chow, J. C., Watson, J. G., Chen, L. W. A., Chang, M. C. O., Robinson, N. F., Trimble, D., and Kohl, S.: The IMPROVE_A temperature protocol for thermal/optical carbon analysis: Maintaining consistency with a long-term database, J. Air Waste Manag. Assoc., 57, 1014–1023, https://doi.org/10.3155/1047-3289.57.9.1014, 2007.

Chow, J. C., Watson, J. G., Robles, J., Wang, X., Chen, L. W. A., Trimble, D. L., Kohl, S. D., Tropp, R. J., and Fung, K. K.: Quality assurance and quality control for thermal/optical analysis of aerosol samples for organic and elemental carbon, Anal. Bioanal. Chem., 401, 3141–3152, https://doi.org/10.1007/s00216-011-5103-3, 2011.

Dal Maso, M., Kulmala, M., Riipinen, I., Wagner, R., Hussein, T., Aalto, P. P., and Lehtinen, K. E. J.: Formation and growth of fresh atmospheric aerosols: Eight years of aerosol size distribution data from SMEAR II, Hyytiälä, Finland, Boreal Environ. Res., 10, 323–336, 2005.

Denjean, C., Formenti, P., Picquet-Varrault, B., Camredon, M., Pangui, E., Zapf, P., Katrib, Y., Giorio, C., Tapparo, A., Temime-Roussel, B., Monod, A., Aumont, B., and Doussin, J. F.: Aging of secondary organic aerosol generated from the ozonolysis of α-pinene: Effects of ozone, light and temperature, Atmos. Chem. Phys., 15, 883–897, https://doi.org/10.5194/acp-15-883-2015, 2015.

Dominick, D., Wilson, S. R., Paton-Walsh, C., Humphries, R., Guérette, E. A., Keywood, M., Kubistin, D., and Marwick, B.: Characteristics of airborne particle number size distributions in a coastal-urban environment, Atmos. Environ., 186, 256–265, https://doi.org/10.1016/j.atmosenv.2018.05.031, 2018.

Fitsiou, E., Pulido, T., Campisi, J., Alimirah, F., and Demaria, M.: Cellular Senescence and the Senescence-Associated Secretory Phenotype as Drivers of Skin Photoaging, J. Invest. Dermatol., 141, 1119–1126, https://doi.org/10.1016/j.jid.2020.09.031, 2021.

Grainger, R. G., Lambert, A., Rodgers, C. D., Taylor, F. W., and Deshler, T.: Stratospheric aerosol effective radius, surface area and volume estimated from infrared measurements, J. Geophys. Res., 100, https://doi.org/10.1029/95jd00988, 1995.

Hamed, A., Joutsensaari, J., Mikkonen, S., Sogacheva, L., Dal Maso, M., Kulmala, M., Cavalli, F., Fuzzi, S., Facchini, M. C., Decesari, S., Mircea, M., Lehtinen, K. E. J., and Laaksonen, A.: Nucleation and growth of new particles in Po Valley, Italy, Atmos. Chem. Phys., 7, 355–376, https://doi.org/10.5194/acp-7-355-2007, 2007.

Hansen, J. E. and Travis, L. D.: Light scattering in planetary atmospheres, Space Sci. Rev., 16, 527–610, https://doi.org/10.1007/BF00168069, 1974.

Hao, Y., Gou, Y., Wang, Z., Huang, W., Wan, F., Tian, M., and Chen, J.: Current challenges in the visibility improvement of urban Chongqing in Southwest China: From the perspective of PM2.5-bound water uptake property over 2015–2021, Atmos. Res., 300, 107215, https://doi.org/10.1016/j.atmosres.2023.107215, 2024.

Hong, J., Ma, J., Ma, N., Shi, J., Xu, W., Zhang, G., Zhu, S., Zhang, S., Tang, M., Pan, X., Xie, L., Li, G., Kuhn, U., Yan, C., Qi, X., Zha, Q., Nie, W., Tao, J., He, Y., Zhou, Y., Sun, Y., Xu, H., Liu, L., Cai, R., Zhou, G., Kuang, Y., Yuan, B., Wang, Q., Petäjä, T., Kerminen, V. M., Kulmala, M., Cheng, Y., and Su, H.: Low Hygroscopicity of Newly Formed Particles on the North China Plain and Its Implications for Nanoparticle Growth, Geophys. Res. Lett., 51, https://doi.org/10.1029/2023GL107516, 2024.

Hussein, T., Puustinen, A., Aalto, P. P., Mäkelä, J. M., Hämeri, K., and Kulmala, M.: Urban aerosol number size distributions, Atmos. Chem. Phys., 4, 391–411, https://doi.org/10.5194/acp-4-391-2004, 2004.

Jung, C. H., Shin, H. J., Lee, J. Y., and Kim, Y. P.: Sensitivity and contribution of organic aerosols to aerosol optical properties based on their refractive index and hygroscopicity, Atmosphere (Basel)., 7, https://doi.org/10.3390/atmos7050065, 2016.

Kerminen, V. M., Chen, X., Vakkari, V., Petäjä, T., Kulmala, M., and Bianchi, F.: Atmospheric new particle formation and growth: Review of field observations, Environ. Res. Lett., 13, https://doi.org/10.1088/1748-9326/aadf3c, 2018.

Kuang, Y., He, Y., Xu, W., Zhao, P., Cheng, Y., Zhao, G., Tao, J., Ma, N., Su, H., Zhang, Y., Sun, J., Cheng, P., Yang, W., Zhang, S., Wu, C., Sun, Y., and Zhao, C.: Distinct diurnal variation in organic aerosol hygroscopicity and its relationship with oxygenated organic aerosol, Atmos. Chem. Phys., 20, 865–880, https://doi.org/10.5194/acp-20-865-2020, 2020.

Kuang, Y., Zhao, C. S., Zhao, G., Tao, J. C., Xu, W., Ma, N., and Bian, Y. X.: A novel method for calculating ambient aerosol liquid water content based on measurements of a humidified nephelometer system, Atmos. Meas. Tech., 11, 2967–2982, https://doi.org/10.5194/amt-11-2967-2018, 2018.

Kuang, Y., Zhao, C., Tao, J., Bian, Y., Ma, N., and Zhao, G.: A novel method for deriving the aerosol hygroscopicity parameter based only on measurements from a humidified nephelometer system, Atmos. Chem. Phys., 17, 6651–6662, https://doi.org/10.5194/acp-17-6651-2017, 2017.

Kulmala, M., Petäjä, T., Nieminen, T., Sipilä, M., Manninen, H. E., Lehtipalo, K., Dal Maso, M., Aalto, P. P., Junninen, H., Paasonen, P., Riipinen, I., Lehtinen, K. E. J., Laaksonen, A., and Kerminen, V. M.: Measurement of the nucleation of atmospheric aerosol particles, Nat. Protoc., 7, 1651–1667, https://doi.org/10.1038/nprot.2012.091, 2012.

Lu, Y., Yan, C., Fu, Y., Chen, Y., Liu, Y., Yang, G., Wang, Y., Bianchi, F., Chu, B., Zhou, Y., Yin, R., Baalbaki, R., Garmash, O., Deng, C., Wang, W., Liu, Y., Petäjä, T., Kerminen, V. M., Jiang, J., Kulmala, M., and Wang, L.: A proxy for atmospheric daytime gaseous sulfuric acid concentration in urban Beijing, Atmos. Chem. Phys., 19, 1971–1983, https://doi.org/10.5194/acp-19-1971-2019, 2019.

Nairn, J. R. and Fawcett, R. J. B.: The excess heat factor: A metric for heatwave intensity and its use in classifying heatwave severity, Int. J. Environ. Res. Public Health, 12, 227–253, https://doi.org/10.3390/ijerph120100227, 2014.

Peng, C., Tian, M., Chen, Y., Wang, H., Zhang, L., Shi, G., Liu, Y., Yang, F., and Zhai, C.: Characteristics, formation mechanisms and potential transport pathways of PM2.5 at a rural background site in Chongqing, Southwest China, Aerosol Air Qual. Res., 19, 1980–1992, https://doi.org/10.4209/aaqr.2019.01.0010, 2019.

Peng, C., Tian, M., Wang, X., Yang, F., Shi, G., Huang, R. J., Yao, X., Wang, Q., Zhai, C., Zhang, S., Qian, R., Cao, J., and Chen, Y.: Light absorption of brown carbon in PM2.5 in the Three Gorges Reservoir region, southwestern China: Implications of biomass burning and secondary formation, Atmos. Environ., 229, 117409, https://doi.org/10.1016/j.atmosenv.2020.117409, 2020.

Rissler, J., Vestin, A., Swietlicki, E., Fisch, G., Zhou, J., Artaxo, P., and Andreae, M. O.: Size distribution and hygroscopic properties of aerosol particles from dry-season biomass burning in Amazonia, Atmos. Chem. Phys., 6, 471–491, https://doi.org/10.5194/acp-6-471-2006, 2006.

Rosati, B., Isokääntä, S., Christiansen, S., Jensen, M. M., Moosakutty, S. P., De Jonge, R. W., Massling, A., Glasius, M., Elm, J., Virtanen, A., and Bilde, M.: Hygroscopicity and CCN potential of DMS-derived aerosol particles, Atmos. Chem. Phys., 22, 13449–13466, https://doi.org/10.5194/acp-22-13449-2022, 2022.

Schkolnik, G., Chand, D., Hoffer, A., Andreae, M. O., Erlick, C., Swietlicki, E., and Rudich, Y.: Constraining the density and complex refractive index of elemental and organic carbon in biomass burning aerosol using optical and chemical measurements, Atmos. Environ., 41, 1107–1118, https://doi.org/10.1016/j.atmosenv.2006.09.035, 2007.

Stein, A. F., Draxler, R. R., Rolph, G. D., Stunder, B. J. B., Cohen, M. D., and Ngan, F.: Noaa's hysplit atmospheric transport and dispersion modeling system, Bull. Am. Meteorol. Soc., 96, 2059–2077, https://doi.org/10.1175/BAMS-D-14-00110.1, 2015.

Strader, R., Lurmann, F., and Pandis, S. N.: Evaluation of secondary organic aerosol formation in winter, Atmos. Environ., 33, 4849–4863, https://doi.org/10.1016/S1352-2310(99)00310-6, 1999.

Tan, F., Zhang, H., Xia, K., Jing, B., Li, X., Tong, S., and Ge, M.: Hygroscopic behavior and aerosol chemistry of atmospheric particles containing organic acids and inorganic salts, npj Clim. Atmos. Sci., 7, 1–21, https://doi.org/10.1038/s41612-024-00752-9, 2024.

Tian, J., Guan, H., Zhou, Y., Zheng, N., Xiao, H., Zhao, J., Zhang, Z., and Xiao, H.: Isotopic source analysis of nitrogen-containing aerosol: A study of PM2.5 in Guiyang (SW, China), Sci. Total Environ., 760, 143935, https://doi.org/10.1016/j.scitotenv.2020.143935, 2021.

Wan, F., Hao, Y., Huang, W., Wang, X., Tian, M., and Chen, J.: Hindered visibility improvement despite marked reduction in anthropogenic emissions in a megacity of southwestern China: An interplay between enhanced secondary inorganics formation and hygroscopic growth at prevailing high RH conditions, Sci. Total Environ., 895, 165114, https://doi.org/10.1016/j.scitotenv.2023.165114, 2023.

Wang, H., Tian, M., Chen, Y., Shi, G., Liu, Y., Yang, F., Zhang, L., Deng, L., Yu, J., Peng, C., and Cao, X.: Seasonal characteristics, formation mechanisms and source origins of PM2.5 in two megacities in Sichuan Basin, China, Atmos. Chem. Phys., 18, 865–881, https://doi.org/10.5194/acp-18-865-2018, 2018.

Wang, Y. Q.: MeteoInfo: GIS software for meteorological data visualization and analysis, Meteorol. Appl., 21, 360–368, https://doi.org/10.1002/met.1345, 2014.

Xu, W., Kuang, Y., Bian, Y., Liu, L., Li, F., Wang, Y., Xue, B., Luo, B., Huang, S., Yuan, B., Zhao, P., and Shao, M.: Current Challenges in Visibility Improvement in Southern China, Environ. Sci. Technol. Lett., 7, 395–401, https://doi.org/10.1021/acs.estlett.0c00274, 2020.

Xue, B., Kuang, Y., Xu, W., and Zhao, P.: Joint increase of aerosol scattering efficiency and aerosol hygroscopicity aggravate visibility impairment in the North China Plain, Sci. Total Environ., 839, 141163, https://doi.org/10.1016/j.scitotenv.2022.156279, 2022.

Zhao, G., Hu, M., Fang, X., Tan, T., Xiao, Y., Du, Z., Zheng, J., Shang, D., Wu, Z., Guo, S., and Zhao, C.: Larger than expected variation range in the real part of the refractive index for ambient aerosols in China, Sci. Total Environ., 779, 146443, https://doi.org/10.1016/j.scitotenv.2021.146443, 2021.

Zhu, Y., Shen, Y., Li, K., Meng, H., Sun, Y., Yao, X., Gao, H., Xue, L., and Wang, W.: Investigation of Particle Number Concentrations and New Particle Formation With Largely Reduced Air Pollutant Emissions at a Coastal Semi-Urban Site in Northern China, J. Geophys. Res. Atmos., 126, 1–20, https://doi.org/10.1029/2021JD035419, 2021.